Magnetic Repulsion-Based Robot With Diverse Locomotion Capabilities

Zihan Wei, *Graduate Student Member, IEEE*, Zongze Li, Yuxuan Xiang, *Graduate Student Member, IEEE*, Jun Liu, and Jiachen Zhang, *Member, IEEE*

***Abstract*—Locomotion is a fundamental capability that all mobile robots strive to achieve. A large variety of magnetic miniature robots have been proposed to leverage the magnetic forces and torques between internal magnetic agents and external magnetic fields to enable various locomotion on different terrains. However, few of them can achieve diverse locomotion capabilities. And their locomotion capabilities depend on specific environments, which hinders their applicability in the real world. This letter presents a magnetic repulsion-based robot (MR ^{2}) with diverse locomotion capabilities, demonstrating agile and robust movement in diverse environments. The MR^2 has two embedded free-to-rotate spherical magnets. The local magnetic force between these two magnets is leveraged to generate reciprocating motions with the help of a pair of one-crease linkages. While, the asymmetrical design of MR^2 transduces this reciprocating motion into controlled directional locomotion. By tuning the global magnetic field, the MR^2 demonstrates non-holonomic mobility and steerability. It can also switch between locomotion modes of crawling, tumbling, and climbing, making it adaptable to diverse terrains and environments. The MR^2 demonstrates a robust locomotion capability with a crawling speed of 84.10 mm $\cdot$ s^{-1} (3.50 bodylength/s), a turning speed of 25.2°/s, a tumbling speed of 68.98 mm $\cdot$ s^{-1} (2.87 bodylength/s) and a climbing ability up a slope of 45°.**

***Index Terms*—Magnetic actuation, miniature robots, multi-terrain locomotion.**

I. Introduction

MAGNETIC miniature robots exhibit captivating locomotion modes in various environments and diverse terrains [1], [2], [3], [4]. These various locomotion capabilities endow the promising potential applications of miniature robots, ranging from biomedical engineering to deep sea and outer space exploration [5], [6], [7], [8]. Especially for soft robots with customized and heterogeneous magnetic moment in different parts of their bodies, the robots can walk [9], [10], [11], roll [2], crawl [12], [13], jump upwards [14], swim in liquid [15], [16], [17], and climb up slopes [18], [19], [20]. However, few robots in these previous studies are capable of multiple distinctive locomotion modes. And most robots move on continuous terrains, including flat surfaces and tubes. Thus, it is difficult for them to adapt to realistic, complex environments, which limits their real-world applicability. Additionally, for these soft robots with dispersed ferromagnetic particles, the constrained content of magnetic particles induces limited magnetic moments. As a result, limited magnetic force and torque generated from these limited magnetic moments would constrain the moving capability of these soft robots, including moving speed, climbing angle, and barrier-overcoming ability. In summary, it is still an open challenge to achieve robust and various locomotion modes with a single miniature robot.

One attempt to address this challenge is introducing origami structures into the magnetic miniature robots to create discontinuous structures, which prompt their flexible locomotion capability. For example, the single unit Krestling magnetic robots can roll, flip, and even swim in the water through spinning [2]. Furthermore, the assembled Krestling structure endows the crawling, steering, narrow space exploring, and drug delivery abilities to magnetic miniature robots [21]. On the other hand, with the help of spring origami structures, the robot could switch between various locomotion modes, including worm crawling, crab crawling, and rolling motion [22], [23]. Integrating with the dispersed magnetic component, the spring origami structure imparts higher velocity (12.01–51.13 mm $\cdot$ s^{-1}) to the robot [22]. Besides these locomotion abilities, even climbing up the wall could be realized by integrating electromagnetic coil and origami structures into the robot [24]. However, in these structures' designs, the limited magnetic forces and complex structures of origami endow challenges to robots' locomotion and fabrication.

To improve the magnetic forces and torques outputting ability, the local forces between two magnetic agents might be a solution for magnetic miniature robots' robust locomotion performances. Impact forces between different robot components are utilized to provide internal vibration to push the robots forward [25], [26], [27]. The wireless resonant magnetic micro-actuator driven by impact mechanical force could reach the speed of 12.5 mm $\cdot$ s^{-1} [28], [29]. Powered by an oscillating magnetic field ($|\boldsymbol{B}|$=2 mT), the soft-magnetic bodies are magnetized and demagnetized frequently. As a result, the induced magnetization of free-moving and fixing parts would attract each other in the uniform magnetic field and separate by spring when the field is turned off. This ultra-fast (2–8 kHz) impacting process motivates the robot to move forward and backward [30]. Furthermore, after changing the gold spring to polymer, the robot's speed could be increased

Manuscript received 18 July 2023; accepted 9 November 2023. Date of publication 20 November 2023; date of current version 28 November 2023. This letter was recommended for publication by Associate Editor X. Liu and Editor X. Liu upon evaluation of the reviewers' comments. This work was supported by the Research Grants Council of the Hong Kong Special Administrative Region, China, under Projects CityU 21202822, CityU 11212321, and CityU 11217922.
(Corresponding authors: Jiachen Zhang; Jun Liu.)

Zihan Wei, Zongze Li, Yuxuan Xiang, and Jiachen Zhang are with the Department of Biomedical Engineering, City University of Hong Kong, Hong Kong SAR, China (e-mail: zihanwei3-c@my.cityu.edu.hk; zongzeli4-c@my.cityu.edu.hk; yxxiang.bme@my.cityu.edu.hk; jzhang.bme@cityu.edu.hk).

Jun Liu is with the Department of Mechanical Engineering, City University of Hong Kong, Hong Kong SAR, China (e-mail: jun.liu@cityu.edu.hk).
This letter has supplementary downloadable material available at https://doi.org/10.1109/LRA.2023.3334557, provided by the authors.

Digital Object Identifier 10.1109/LRA.2023.3334557

2377-3766 © 2023 IEEE. Personal use is permitted, but republication/redistribution requires IEEE permission.
See https://www.ieee.org/publications/rights/index.html for more information.

Authorized licensed use limited to: The University of Hong Kong Libraries. Downloaded on October 03,2024 at 16:21:31 UTC from IEEE Xplore. Restrictions apply.

to 20 mm · s^{-1} [27]. Although, with high-speed performance, it is difficult to steer this kind of robot. Thus, this kind of inner force leads to limited locomotion and environment adaptability of the magnetic robot.

With a similar principle, a vibro-impact self-propelled capsule robot can move forward while actuated by the impact between the inside magnets and the fixed spring of the capsule [26], [31], [32]. The magnetic field pushes the "hammer" (magnets) to hit the capsule, propelling the robot to move a short distance. By designing four inner electromagnetic coils, the changing magnetic field would navigate the magnet's "hammer" to hit the intended location inside the capsule. As a result, the vibro-impact robot could be steered in the horizontal plane and achieve a moving speed of 13.47 mm · s^{-1} at 30 Hz. Nonetheless, the robot still has a limited steering capacity of a turning speed of 4.4°/s, which constrains its application in complex environments. In summary, the inner forces in robots could be leveraged to achieve robust locomotion. In addition, the local magnetic repulsion forces between magnets would generate the robust relative motion between them through tuning their magnetic moment angles [33].

In this work, a magnetic repulsion-based robot (MR^2) is proposed with diverse locomotion capabilities, including earthworm-like crawling, turning, caterpillar-like tumbling, and inchworm-like climbing. The local magnetic force between two embedded free-to-rotate spherical magnets is leveraged to generate reciprocating motions with the help of a pair of one-crease linkages. The asymmetrical design of the MR^2's feet transduces this reciprocating motion into controlled directional locomotion. By tuning the global magnetic field, the MR^2 could switch between locomotion modes including crawling, turning, tumbling and climbing, making it adaptable to diverse terrains and environments. The magnetic robot demonstrates a robust locomotion capacity with crawling velocity exceeding 84.10 mm· s^{-1}, a turning speed of 25.2°/s, and a climbing ability up a 45° slope.

II. Design of the Magnetic Repulsion-Based Robot

This section explains the structure and the working principles of the proposed MR^2. The three parts of MR^2, including magnetic units, origami-inspired one-crease linkages, and asymmetrical feet, are introduced. And the local magnetic interaction forces are illustrated to explain the working principle of MR^2's locomotion.

A. *Structure of Magnetic Repulsion-Based Robot*

As shown in Fig. 1(a), the MR^2 (2.3 g) maintains a length of 24 mm (locking state), a width of 9 mm, and a height of 8.8 mm, while the length can transfer to 41.2 mm at the opening state. The MR^2 consists of three components: magnetic units with embedded spherical magnets, origami-inspired one-crease linkages, and Polydimethylsiloxane (PDMS, $SYLGARD184$) feet. When exerted by an external magnetic field, the spherical magnets (diameter: 4.76 mm, magnetic moment: 0.0506 Am^2, magnetization: 8.95×10^5 A/m, K&J Inc.) can freely rotate inside the separated wells of MR^2. The local magnetic force between them changes according to the angle θ enclosed by magnets' magnetic moment $\boldsymbol{m}$ and the separation vector $\boldsymbol{r_{12}}$ pointing from magnet 1 to magnet 2, as shown in Fig. 1(c) and (d). In this way, the distance between two magnets would be changed when θ is altered by the external magnetic field's torque. In summary, these two magnets transduce the magnetic field energy into relative motion between the two magnetic units.

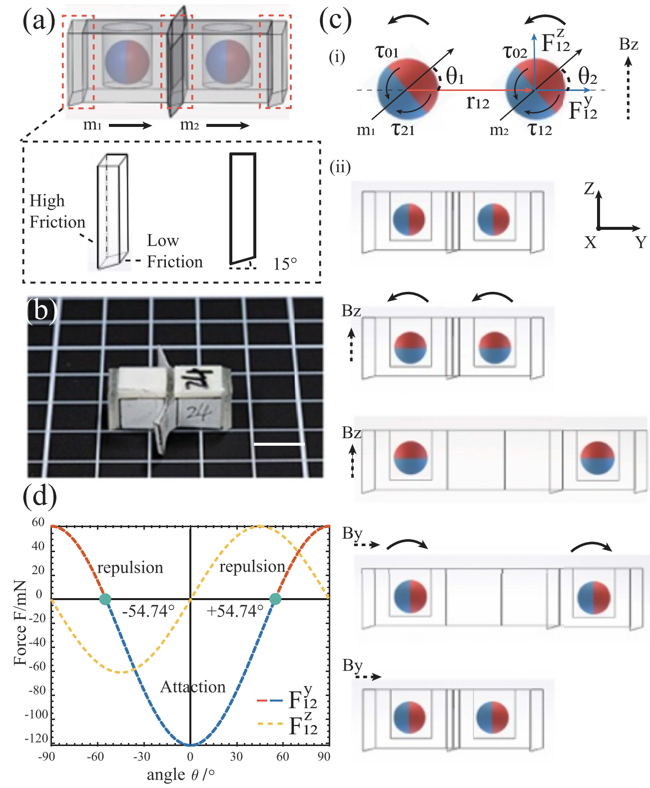

Fig. 1. Structure and mechanism of the proposed MR^2. (a) A Transparent schematic of MR^2 in locking state and detail of PDMS feet. The red and blue colors denote the north and south poles of the embedded spherical magnets, respectively. The arrow denotes the direction of the magnetic moment of the spherical magnets. In the zoom-in figure, the 3D view of the feet with friction distribution is shown in the left picture, and the side view of the asymmetrical design is shown in the right one. (b) A photograph of MR^2 corresponding to the schematic in (a). The scale bar is 10 mm. (c) The working principle of the reciprocating motion between the two embedded spherical magnets. (i) The force and torque on spherical magnets generated by the global magnetic field and another spherical magnet. The separation vector pointing from magnet 1 to 2 is denoted by $\boldsymbol{r_{12}}$. θ_i denotes the local angle between the magnetic moment and the separation vector. $\boldsymbol{F^y_{12}}$ and $\boldsymbol{F^z_{12}}$ denote the radial and tangential forces on magnet 2 generated by magnet 1. $\boldsymbol{\tau_{12}}$ and $\boldsymbol{\tau_{02}}$ denote the torque applied on magnet 2 from magnet 1 and global magnetic field. (ii) The kinematics of the MR^2's reciprocating motion. The solid line arrow denotes the rotation direction of the spherical magnets, and the dashed line arrows denote the orientation of the magnetic field. (d) The local magnetic forces versus local angles (θ) of the spherical magnets.The line that consist of red and blue section denotes the radial force $\boldsymbol{F^y_{12}}$ between spherical magnets. The red denotes the repulsion force, and blue denotes the attraction force. The yellow line denotes the tangential force between spherical magnets. The green dots denote the zero radial force at $\theta_i = \pm 54.74°$.

A pair of origami-inspired linkages (length of the opening state: 20 mm, width: 7 mm) bridge the separated anterior and posterior magnetic units of MR^2 to transform the local magnetic force into reciprocating motion. The linkage is fabricated by folding A4 paper (80 gsm, thickness: 104 μm) into one crease and glued to the magnetic units, as shown in Fig. 1(a). The length of the linkages could change from 20 mm (unfolded state) to 0.23 mm (folded state) along $\boldsymbol{r_{12}}$, which endows the suitable distance range for two spherical magnets to generate proper local magnetic forces and an excellent extension ratio of 86.96.

Authorized licensed use limited to: The University of Hong Kong Libraries. Downloaded on October 03,2024 at 16:21:31 UTC from IEEE Xplore. Restrictions apply.

To transfer the reciprocating motion of MR^2 into controlled directional movement, the asymmetrical structure of the PDMS feet (length: 9 mm, width: 1.6 mm, height: 7.8 mm) is designed with friction distribution as shown in Fig. 1(a). The asymmetrical design of the PDMS feet is optimized after experimenting with various shapes, angles, and materials, including hard paper, Polyvinyl chloride (PVC), Polyimide (PI), Poly Lactic Acid (PLA), and PDMS. The friction distribution of the asymmetrical PDMS feet is generated by a foot slope with 15° between the ground and foot surface with different contact areas, as shown in the side view of the PDMS feet in Fig. 1(a). Ascribed to different contact areas, the high-friction portion (long side of the foot) of PDMS feet can anchor on various terrains, prohibiting backward slide during the forward movement, while the low-friction portion (slope surface) permits smooth forward motion. Furthermore, two PDMS feet are attached to the anterior unit of MR^2 to generate enough friction to anchor on the ground, ensuring dragging the posterior unit forward during the contraction process. While, the posterior unit is attached with one foot at the robot's end, preventing the robot from sliding back during the elongation process and enabling smooth movement during the contraction process. Finally, the MR^2 is fabricated by embedding the spherical magnets into the hollow wells in magnetic units and attaching these units with linkages and feet with glue, as shown in Fig. 1(b).

B. Working Mechanism of Magnetic Repulsion-Based Robot

This work employs the local magnetic interaction forces between two embedded magnets as the motivating sources for the proposed MR^2 to enable robust and diverse locomotion. This local magnetic interaction force would change from attractive to repulsive when the local angle θ is larger than 54.74° in close proximity [34]. Herein, utilizing the magnetic torque applied by the global magnetic field can modulate the directions of the $\boldsymbol{m}$ of embedded spherical magnets, resulting in the generation of both an altering force and a changing relative displacement, as shown in Fig. 1(c).

During this process, we assume the two spherical magnets are always aligned with the direction of the external magnetic field $\boldsymbol{B_g}$ since magnetic torque generated by $\boldsymbol{B_g}$ is strong enough to override the torque generated by another spherical magnet. Thus, both spherical magnets have the same local orientation angle θ, as shown in Fig. 1(c)-(i). The magnetic torque $\boldsymbol{\tau}$ exerted by the global magnetic field or magnet 1 on spherical magnet 2 is

$$\boldsymbol{\tau_{i2}} = \mathbf{m_2} \times \mathbf{B_i} \tag{1}$$

where $\mathbf{m_2}$ is the magnetic moment of the spherical magnet 2, $\mathbf{B_i}$ is the magnetic flux density of the global magnetic field or magnet 1. From the magnetic dipole model, there is the magnetic flux density $\boldsymbol{B_{12}}$ at position of magnet 2 generated by magnet 1

$$\mathbf{B_{12}} = \frac{\mu_0}{4\pi r_{12}^3}\left(\frac{3\left(\mathbf{m_1}\cdot\mathbf{r_{12}}\right)\mathbf{r_{12}}}{r_{12}^2} - \mathbf{m_1}\right) \tag{2}$$

where $\mu_0 = 4\pi \times 10^{-7}$ H/m is the vacuum permeability. Substituting (2) and global magnetic field $\boldsymbol{B_g}$ into (1), the value of the magnetic torque $\boldsymbol{\tau_{12}}$ and $\boldsymbol{\tau_{02}}$ applied on magnet 2 generated by magnet 1 and the global magnetic field are

$$\tau_{12}^x = -\frac{3\mu_0 m_1 m_2}{8\pi r_{12}^3}\sin 2\theta \tag{3}$$

$$\tau_{02}^x = m_2 B_g \cos\theta \tag{4}$$

When $|\tau_{02}^x| \geq |\tau_{12}^x|$, in this work, when the value of $\boldsymbol{B_g}$ is larger than 12.7 mT, the spherical magnets can rotate to align with the global magnetic field resulting in the changing local magnetic forces. The local magnetic force $\mathbf{F}$ between the two spherical magnets is described by

$$\mathbf{F} = \left(\mathbf{m}\cdot\nabla\right)\mathbf{B_{12}} \tag{5}$$

where ∇ is the gradient. Since the global magnetic field employed in this work is uniform within the workspace, its gradient is zero and thus not included in (5). Furthermore, in the initial state, the separation vector ($\boldsymbol{r_{12}}$) is aligned with the y-axis. Thus, the radial F_{12}^y and tangential forces F_{12}^z on magnet 2 generated by magnet 1 are shown by substituting the (2) into (5).

$$F_{12}^y = \frac{3\mu_0 m_1 m_2}{4\pi r_{12}^4}\left(1 - 3\cos^2\theta\right) \tag{6}$$

$$F_{12}^z = \frac{3\mu_0 m_1 m_2}{4\pi r_{12}^4}\sin\left(2\theta\right) \tag{7}$$

The values of F_{12}^y and F_{12}^z are illustrated in Fig. 1(d). When $|\theta| \geq 54.74°$, the spherical magnets would mutually repulse to break the locking state. The maximum repulsive force of $\boldsymbol{F_{12}^y}$ could achieve 60.8 mN, which is way larger than the gravity of the MR^2 (22.6 mN). When the $|\theta| \leq 54.74°$, the two spherical magnets in the MR^2 would attract each other and resume MR^2 to locking state.

As a result, the reciprocating motion of the MR^2 is realized by tuning the global magnetic field $\boldsymbol{B_g}$ as illustrated in Fig. 1(c)-(ii). At first, the MR^2 stays at a locking state, (10.6 mm between two spherical magnets), while the angle θ is zero degree. Then, when the global magnetic field $\boldsymbol{B_z}$ is applied, the spherical magnets would be rotated by magnetic torque τ_{0i}^x to align their $\mathbf{m}$ with $\boldsymbol{B_z}$. During this process, when the angle θ is beyond 54.74°, the locking state of the MR^2 would be broken and transformed into an opening state until the linkage constrains the two magnets' distance. Next, when the $\boldsymbol{B_g}$ disappears or changes to the $\boldsymbol{B_y}$, the magnetic torque from another magnet or $\boldsymbol{B_g}$ would rotate the spherical magnet's $\boldsymbol{m}$ to realign with $\boldsymbol{r_{12}}$. Thus, the attractive force would resume the MR^2 to the locking state as θ decreases smaller than 54.74°.

Furthermore, with the help of the distance constraint effect of the origami-inspired linkages and the friction distribution of the PDMS feet, the reciprocating motion of the MR^2 is transduced into controlled directional motion. As a result, the MR^2 possesses earthworm-like crawling locomotion.

III. Diverse Locomotion Capabilities of Magnetic Repulsion-Based Robot

Under the actuation and control of different profiles of the global magnetic field, the proposed MR^2 shows diverse locomotion capabilities, including crawling, turning, climbing, and tumbling on various terrains with amphibious performance.

A. Crawling Motion

1) *Locomotion Kinematics:* The proposed MR^2 can crawl by integrating the local magnetic force between the two spherical magnets, the distance constraint of linkages, and asymmetric friction distribution of its feet, as shown in Figs. 2(a) and 3(a). This local magnetic interaction force is

Authorized licensed use limited to: The University of Hong Kong Libraries. Downloaded on October 03,2024 at 16:21:31 UTC from IEEE Xplore. Restrictions apply.

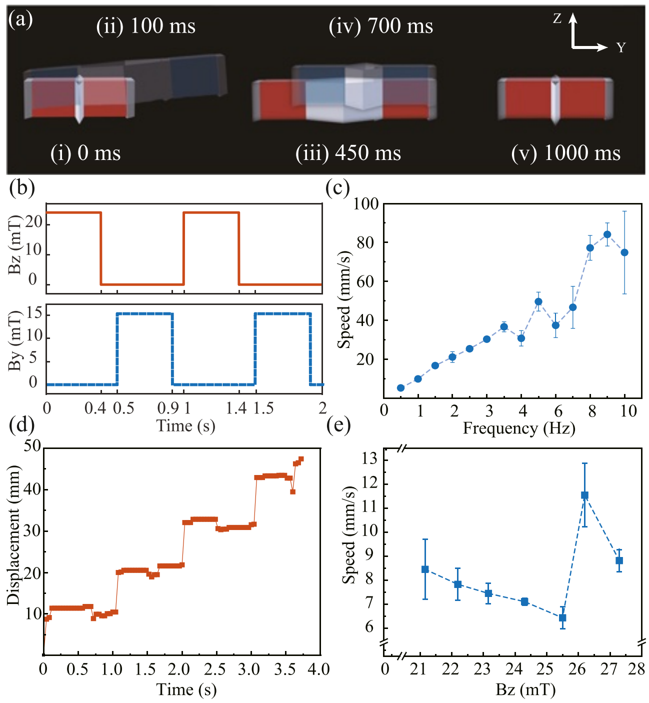

Fig. 2. Kinematics of the proposed MR^2 crawling motion (a) A schematic illustrating the crawling motion of MR^2 on a flat surface. The red and blue colors denote the initial and final states of MR^2 at each location. (b) Profiles of the global magnetic field components along the z and y axis. (c) The crawling speed of MR^2 varies with the magnetic field frequency. Each data point represents the average value of speed trials, and the error bar stands for the standard deviation. (d) The displacement of MR^2 along the y-axis during the crawling process. (e) The crawling speed of MR^2 varies with the magnetic field flux density along the z-axis. Each data point represents the average value of speed trials, and the error bar stands for the standard deviation.

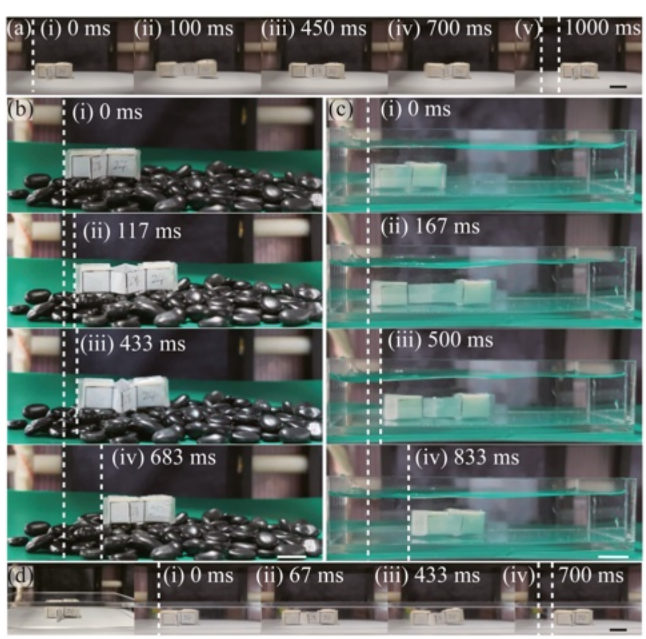

Fig. 3. Crawling motion of the proposed MR^2 in diverse environments. (a) The photographs illustration of MR^2's crawling motion on a flat surface. (b) Crawling motion of MR^2 on the rock. (c) Crawling motion of MR^2 in water. (d) Crawling motion of MR^2 in narrow spaces. All scale bars are 10 mm.

modulated by $\boldsymbol{B_g}$ to motivate MR^2's crawling locomotion, as shown in Fig. 2(b). The $\boldsymbol{B_z}$ and $\boldsymbol{B_y}$ with rectangular profile are $\boldsymbol{B_g}$'s components in the z-axis and y-axis actuating the repulsive and attractive forces between the magnets. The equations of their rectangular profiles are shown as follows:

$$B_z = \begin{cases} A_z & 0 \le t < 0.4T \\ 0 & 0.4T \le t < T \end{cases} \tag{8}$$

$$B_y = \begin{cases} A_y & 0.5T \le t < 0.9T \\ 0 & 0 \le t < 0.5T \text{ and } 0.9T \le t < T \end{cases} \tag{9}$$

where A_z and A_y are the amplitudes of the $\boldsymbol{B_z}$ and $\boldsymbol{B_y}$, respectively. T is the period, which is 1 s in Fig. 2(b). The rectangular wave in the z-axis and y-axis have the same frequency and same duty cycle (40%) but exist a half-period phase difference. To prevent the induction effects of the electromagnetic coil, there are 10% of the blank segment in the period after the B_z or B_y.

The half-period phase difference between B_z and B_y enables the direction change of the global magnetic field in one period, which leads to the extension and contraction of the MR^2. At first, when $\boldsymbol{B_z}$ is applied to the robot, the MR^2 breaks the locking state and extends the anterior unit from state (i) to state (ii), as shown in Fig. 2(a). It takes 100 ms for the anterior unit to extend and reach the opening state. Then, this opening state will keep until 450 ms when $\boldsymbol{B_z}$ decreases to 0 mT. In the second stage, the two embedded magnets realign to each other along $\boldsymbol{r_{12}}$ after the disappearance of the magnetic field in the z-axis at 450 ms. Thus, the MR^2 starts to contract after this moment while accelerating the contraction process when $\boldsymbol{B_y}$ of 15.35 mT is applied after 500 ms. The whole contraction process lasts 250 ms from state (iii) to state (iv), and then, MR^2 resumes the locking state (state v) and keeps it until the next period.

By repeating the period mentioned above, the crawling locomotion of the proposed MR^2 shows periodic step-like kinematics with a stride length of 10.59 mm at 1 Hz, as shown in Fig. 2(d) and Fig. 3(a). The displacement of the anterior unit in the y-axis shows that MR^2 extends when $\boldsymbol{B_z}$ actuates MR^2 and slides back slightly during the contraction process within a brief timeframe. Then, for the majority of the time, MR^2 stays in the locking or opening state without movement and displacement, as shown in Fig. 2(d).

The crawling speed of MR^2 would be affected by the frequency of $\boldsymbol{B_g}$, as shown in Fig. 2(c). The speed of MR^2 keeps an approximately linear relationship with an increasing frequency below 3.5 Hz from 5.17 mm$\cdot$ s^{-1} to 36.61 mm $\cdot$ s^{-1}, and oscillates when the frequency exceeds 3.5 Hz. This is caused by the balance between the extension time (100 ms), contraction time (250 ms) of MR ^{2} and the actuating frequency, in which the MR^2 maintains the largest step when the frequency is less than 3.5 Hz. However, when the frequency surpasses 3.5 Hz, the actuation time of B_z would be less than 100 ms in a period, which makes the MR^2 unable to extend to its most considerable stride. The extension of the MR^2 can not keep pace with the fast actuating signal. There will be a balance between the stride length and the frequency during extension, resulting in the speed vibration of the MR^2. Although the

Authorized licensed use limited to: The University of Hong Kong Libraries. Downloaded on October 03,2024 at 16:21:31 UTC from IEEE Xplore. Restrictions apply.

stride decreases, ascribed to 1D reciprocation induced by local magnetic force and large extension ratio of the linkage, the MR^2 can achieve a speed beyond 84.10 mm$\cdot$ s^{-1} (3.50 bodylength/s) at 9 Hz, which is way larger than previous research [22].

Besides frequency, the value of $\boldsymbol{B_z}$ is another factor to affect the crawling performance of MR ^{2}, as shown in Fig. 2(e). Only when $\boldsymbol{B_g}$ is strong enough ($B_z \geq 21.16$ mT as a threshold), the generated torque can break the locking state of MR^2. As the augmentation of $\boldsymbol{B_z}$ at 1 Hz, the MR^2's speed declines from 8.46 mm$\cdot$ s^{-1} to 6.44 mm $\cdot$ s^{-1} and achieves the maximum value of 11.55 mm $\cdot$ s^{-1}, finally, achieving 8.83 mm $\cdot$ s^{-1} at 27.29 mT, as shown in SI: Video 5. We assume this phenomenon is attributed to the the balance between stride and global magnetic field $\boldsymbol{B_z}$. Given the (4), the larger magnetic field augments the magnetic torque, thereby enhancing the magnets' angular velocity. Thus, a stronger local force generated by a larger angle θ will actuate the greater stride. However, when the magnetic field is beyond 27 mT, the considerable angular velocity renders the direction oscillation of $\boldsymbol{m}$ near $\boldsymbol{B_z}$. Thus, the speed decreases when $\boldsymbol{B_z}$ is larger than 27 mT. However, the standard deviation (SD: 1.62 mm $\cdot$ s^{-1}) of the speed affected by $\boldsymbol{B_z}$ is way smaller than the SD (24.97 mm $\cdot$ s^{-1}) of speed affected by the frequency. While the SD of the speed affected by $\boldsymbol{B_y}$ is 1.03 mm $\cdot$ s^{-1}. This means frequency weights more in affecting the crawling performance of MR^2.

2) *Crawling in Diverse Environments:* Because of the large local interaction force between the adjacent magnets, the MR ^{2} can not only crawl on a flat surface but also in other more challenging environments, including rocks, water, and narrow space, as shown in Fig. 3 (SI: Video 1). The crawling locomotion of MR^2 on a flat surface is shown as Fig. 3(a) with a stride of 10.59 mm at 1 Hz. Fig. 3(b), (i)–(iv) shows the crawling locomotion of MR^2 on rocks. The origami-inspired linkages and elastic PDMS feet confer remarkable flexibility upon the robot, enabling it to adapt to the discontinuous rocky terrain with diverse surface undulation. The varying frictions between the PDMS feet and the undulating surface morphology of rocks make MR^2 take 117 ms to finish the extending process and 250 ms to drag the posterior body forward. The crawling speed (6.28 mm$\cdot$ s^{-1}) of MR^2 on rocks is lower than that on a flat surface at 1 Hz. This is attributed to the rugged terrain that impedes MR^2's forward movement. However, the robot has a larger stride length of 12.92 mm compared with crawling on a flat plane.

In addition to crawling on undulating rock terrain, the MR^2 demonstrates the amphibious capacity to crawl underwater, as shown in Fig. 3(c), (i)–(iv). Hydrophobic paper is used as linkages to enhance MR^2's adaptability to water. It takes 167 ms for MR^2 to finish the extending process and keep opening until the global magnetic field changes from the z-axis to y-axis in 500 ms. However, different from crawling in the air, 333 ms is needed for MR^2 to resume the locking state. This is due to the higher viscosity and density of water compared with air, which necessitates the expenditure of additional energy and time to expel water between the two magnetic units. During this process, the counter-force of the expelling water even pushes MR^2 to float in water. The lubrication effect of water endows smoother crawling motion and the larger stride of 13.52 mm to MR^2 in water.

Because of the robust crawling locomotion, the MR^2 exhibits adaptability to confined spaces, as shown in Fig. 3(d). The upper wall of the narrow space constraints the extending process of MR^2, resulting in a shorter time (67 ms) for the extension process and longer time (267 ms) to resume the locking state. As a result, the stride length of crawling in narrow spaces is 7.91 mm.

Additionally, the MR^2 is capable of crawling up a gentle slope ($\leq 5°$). The MR^2's crawling motion on diverse terrains demonstrates its versatile and resilient adaptability to complex environments, encompassing both aquatic and atmospheric conditions.

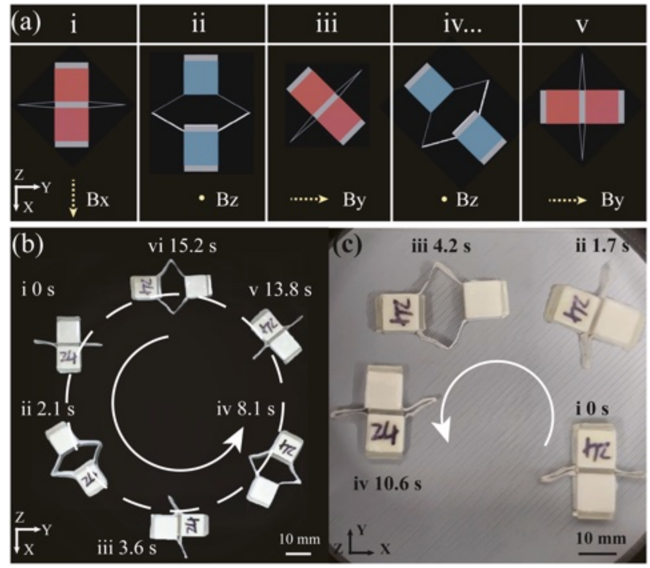

Fig. 4. Turning locomotion of the proposed MR^2. (a) Schematic illustration of the turning motion of MR^2. The red and blue colors denote the initial and final states of MR^2 at each location. (b) Top view photographs of MR^2 in a 360° turn. The scale bar is 10 mm. (c) Top view photographs of MR^2 in a "C" path turning on a slope of 5°. The scale bar is 10 mm.

B. Turning Motion

1) *Locomotion Kinematics:* Besides crawling along one-dimensional (1D) directions, MR^2 could also turn in two-dimensional (2D) planes. In the turning locomotion of MR^2, the global magnetic field's profiles are the same as the profiles of crawling locomotion. However, to achieve turning locomotion, the horizontal components of $\boldsymbol{B_g}$ necessitate the direction changes between the x-axis and y-axis, as shown in Fig. 4(a) (i)–(v). For example, when the horizontal component of $\boldsymbol{B_g}$ changes from the $\boldsymbol{B_x}$ to $\boldsymbol{B_y}$, MR^2 would first extend in the next period actuated by $\boldsymbol{B_z}$. Then, it begins to contract while $\boldsymbol{B_z}$ disappears. In this contraction process, the two spherical magnets tend to align their magnetic moments to the $\boldsymbol{r_{12}}$. Subsequently, while $\boldsymbol{B_y}$ is applied to MR^2, the generated magnetic torque turns the robot body swiftly to the y-axis. Nonetheless, turning MR^2 90° from the x direction to the y direction typically spans four or five periods. In most periods, the MR^2 undergoes only a minor rotational adjustment ($\sim 10°$). While, it performs one significant turning

Authorized licensed use limited to: The University of Hong Kong Libraries. Downloaded on October 03,2024 at 16:21:31 UTC from IEEE Xplore. Restrictions apply.

motion in a large angle (42.82°–55.19°). Completing a 90° turn requires 3.6 s at a turning speed of 25°/s at 1 Hz.

2) *Turning Locomotion in a Circular Paths:* The MR^2 shows an agile turning ability in the x-y plane in a circular path, as shown in Fig. 4(b) (SI: Video 2). The MR^2 initially crawls along the x-axis. When the global magnetic field is switched to the y-axis, the MR^2 turns from the x-axis to the positive direction of the y-axis in 3.6 s around its anterior unit. During this turning process, the anterior unit of MR^2 anchors on the substrate as the rotational center because of the larger friction, while the posterior unit rotates around the anterior unit. Following the transition from the x-axis to the y-axis, the MR^2 proceeds to crawl along the positive direction of the y-axis. Subsequently, when the global magnetic field is switched to the negative direction of the x-axis, the MR^2 undergoes a repeated turning process to align itself with $-\boldsymbol{B_x}$. Finally, after turning to the negative direction of the y-axis, the MR^2 generates a circular path in the x-y plane. In addition, the MR^2 also demonstrates a robust turning ability as a "C" path on a slope of 5°, as shown in Fig. 4(c).

C. Tumbling Motion

1) *Locomotion Kinematics:* In addition to moving in 2D space, MR^2 exhibits a tumbling ability in 3D space when the profile of $\boldsymbol{B_g}$ changes from rectangular wave to rotating wave, as shown in Fig. 5(b). The rotating global magnetic field is the superposition of the cosine and sine wave of $\boldsymbol{B_z}$ and $\boldsymbol{B_y}$, as shown in (10) and (11).

$$B_z = A_z \cos(\omega t) \qquad 0 \le t < T. \tag{10}$$

$$B_y = A_y \sin(\omega t) \qquad 0 \le t < T. \tag{11}$$

where A_z (12.38 mT) and A_y (7.68 mT) are the amplitudes of B_z and B_y. ω is the angular frequency of the B_z and B_y. The B_z and B_y share the same period and frequency. By exchanging the profiles of $\boldsymbol{B_z}$ and $\boldsymbol{B_y}$, the MR^2 would perform the forward and backward tumbling motion in response.

The tumbling locomotion's magnetic flux density is insufficient to disengage the locking state of MR^2. Consequently, the MR^2's two magnetic units function as a unified body with its net magnetic moment always aligned with $\boldsymbol{r_{12}}$. The magnetic torque between the rotating magnetic field $\boldsymbol{B_g}$ and the MR^2's net magnetic moment rotates the MR^2 around in the y-z plane, as shown in Fig. 5(a). The MR^2 undergoes a 360° rotation in a period. Initially propelled by $\boldsymbol{B_z}$ at its wave peak, MR^2 stands upright induced by the magnetic torque spanning 133 ms. Subsequently, as the global magnetic field undergoes a reduction of B_z while with the increase of B_y, the $\boldsymbol{B_g}$ rotates clockwise towards the positive direction of the y-axis. Therefore, the MR^2 undergoes a clockwise tumbling motion of 180° propelled by the global magnetic torque in 467 ms, as shown in Fig. 5(a). Then, the following half period would repeat this process, thereby restoring MR^2 to its original posture at 2π. This periodic rotation process is explicit in the displacement of the center of the mass of MR^2, as shown in Fig. 5(c). The MR^2 oscillates at the peak of its path, attributed to the mismatch of the rotating velocity between MR^2 and $\boldsymbol{B_g}$. During this tumbling

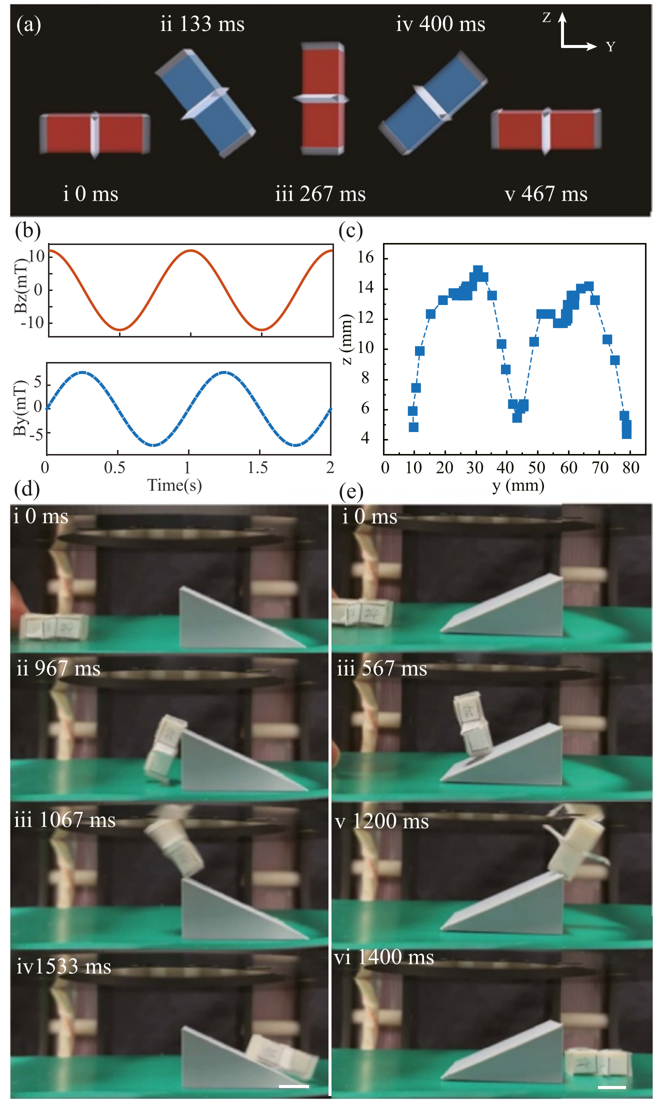

Fig. 5. Tumbling locomotion of the proposed MR^2. (a) A schematic illustrating the tumbling motion of MR^2. The red color denotes the horizontal and vertical gesture of the MR^2, and the blue color denotes the process between them. (b) Profiles of the global magnetic field component of the tumbling locomotion along the z-axis and y-axis. (c) The displacement of MR^2 in the $y-z$ plane in tumbling locomotion. (d) The tumbling locomotion of MR^2 over a 20 mm height barrier. (e) The tumbling locomotion of MR^2 over a 25° slope. All the scalar bars are 10 mm.

locomotion, MR^2 exhibits a stride of 68.98 mm with a speed of 68.98 mm· s^{-1} (2.87 bodylength/s) at 1 Hz.

2) *Tumbling Locomotion on Different Terrains:* Because of the rotation kinematics above, the tumbling locomotion endows the robust and speedy explorations capability to MR^2 on complex and rugged terrains, including barriers and slopes, as shown in Fig. 5 (SI: Video 3). During the tumbling locomotion, the PDMS feet play a key role as an anchoring element, which helps MR^2 tumble over various barriers, as shown in Fig. 5(d). In the first half period, the PDMS feet of MR^2 are oriented backward to the barrier at the standing state, thereby impeded by the barrier. However, in the second half period, these PDMS feet anchor the barrier while the feet pivot to face the

Authorized licensed use limited to: The University of Hong Kong Libraries. Downloaded on October 03,2024 at 16:21:31 UTC from IEEE Xplore. Restrictions apply.

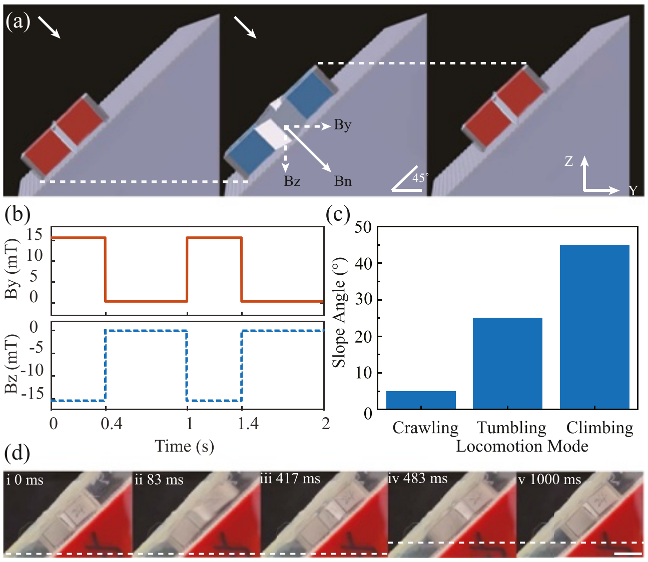

Fig. 6. Climbing locomotion of MR^2. (a) A Schematic illustrating the climbing motion of MR^2. The white arrow denotes the direction of the applied global magnetic field. (b) Profiles of the global magnetic field component along the y and z axis of MR^2's climbing motion for a slope of 45°. (c) The slope angle that MR^2 climbs up in different locomotion. (d) The climbing locomotion of MR^2 on a 45° slope. The scale bar is 10 mm.

barrier. The anchoring ability of the feet helps MR^2 rotate around the contacting point of the feet and the barrier until it tumbles over it. As a result, MR^2 exhibits the robust tumbling capability to conquer the undulating terrain, even the barrier with the similar height (20 mm) as MR^2's body length. In addition to the barrier, the MR^2 demonstrates the tumbling ability over the steeper slope (25°) than the crawling motion (5°), as shown in Fig. 5(e).

D. Climbing Motion

The robust local magnetic forces endow an outstanding climbing performance (climb up a slope of 45°) to MR^2. To motivate the climbing motion of MR^2, a normal global magnetic field to the robot is established to provide sufficient magnetic force and torque to break the locking state. Different from $\boldsymbol{B_g}$ of crawling locomotion, this normal global magnetic field is composed of $-\boldsymbol{B_z}$ and $+\boldsymbol{B_y}$, sharing identical period and phase, as shown in Fig. 6(a) and (b). Specifically, the $\boldsymbol{B_g}$ of climbing the 45° slope is shown as (12) and (13). Its magnetic field components along the negative direction of the z-axis and the positive direction of the y-axis possess the same amplitude value (15.35 mT). Herein, the net magnetic field orients to the -45° normal to the slope.

$$B_z = \begin{cases} -A_z & 0 \leq t < 0.4T \\ 0 & 0.4T \leq t < T \end{cases} \tag{12}$$

$$B_y = \begin{cases} A_y & 0 \leq t < 0.4T \\ 0 & 0.4T \leq t < T \end{cases} \tag{13}$$

As a result, when $\boldsymbol{B_g}$ is exerted, the two spherical magnets rotate along with the applied magnetic field to disrupt the locking state. The anterior unit of MR^2 extends against the gravity and friction at 83 ms, as shown in Fig. 6(d) (SI: Video 4), while the posterior feet anchor in the choppy slope to prevent MR^2 from sliding downwards. Attributed to gravity and friction, the MR^2 costs less time in the extending process with less stride length than that in crawling locomotion. Then, until 400 ms, when $\boldsymbol{B_g}$ is removed, the local magnetic forces resume the MR^2 to the locking state. During this progression, the anterior feet of MR^2 anchor in the step against the backward sliding, while dragging the posterior magnetic unit upwards by the local attraction forces in 66 ms. Subsequently, the MR^2 keeps the locking state until the next period (1000 ms), as shown in Fig. 6(d). The stride during the whole process is 5.93 mm, which helps the robot climb up 4.19 mm along the vertical direction. By changing the amplitude of magnetic flux density in the z-axis and y-axis, separately, the global magnetic field direction and magnitude can be tuned for various slopes. In this work, the maximum angle of slope that MR^2 can climb is 45° in climbing locomotion, which is way larger than the 5° and 25°, in the crawling locomotion and the tumbling locomotion, as shown in Fig. 6(c).

TABLE I
DIVERSE LOCOMOTION OF THE MR^2

Motion	Speed (mm/s)	Signal Wave	Magnetic field (mT)
Crawling on the plane	84.10	Rectangular	Z,Y;25.62,15.35; 9 Hz
Steering on the plane	25.2°/s	Rectangular	Z,Y,X;25.62,15.35,2.68; 1 Hz
Tumbling on the plane	68.98	Sinusoidal	Z,Y; 12.38, 7.68; 1 Hz
Climbing on 45°slope	0.98	Rectangular	Z,Y; 15.35, 15.35; 1 Hz

TABLE II
COMPARISON OF MAGNETIC CRAWLING ROBOTS

Ref.	Year	Speed (mm/s)	Speed (body length/s)	Weight (g)	Magnetic field
This work	2023	84.10	3.50	2.3	25.62 mT, 9 Hz
[22]	2022	12.01	0.34	2.1	8 mT, 3 Hz
[21]	2022	13.2	0.47	0.95	40 mT, 5 Hz
[13]	2019	34	0.56	2.4	30 mT, 3.3 Hz
[10]	2018	28.6	1.68	0.04	200 mT, 16 Hz

E. Disccusion

Above all, the capabilities of MR^2's diverse locomotion are presented in Table I. The primary distinction between the tumbling and crawling modes of the MR^2 is the different exerted global magnetic fields. Furthermore, other waveforms are also investigated, including triangular waves and sawtooth waves. They actuate the MR^2 to perform a similar motion as tumbling. However, this motion is not as continuous as tumbling under sinusoidal waves. The performance of this work and previous studies in recent years are illustrated in Table II. Both average speed and normalized speed are comparable or superior to these preceding works.

IV. CONCLUSION

This work presents a magnetic repulsion-based robot (MR ^{2}) with diverse locomotion capabilities on various terrains. The MR^2 is proposed with two free-to-rotate spherical magnets, and their local magnetic force can be leveraged to generate relative movement. Integrating the constraint functions of a pair of linkages and the asymmetrical design of the PDMS

Authorized licensed use limited to: The University of Hong Kong Libraries. Downloaded on October 03,2024 at 16:21:31 UTC from IEEE Xplore. Restrictions apply.

feet, the relative movement between the two spherical magnets can be transformed into reciprocating motion and further into controlled directional locomotion of MR^2. Through tuning the global magnetic field, the MR^2 could switch between various locomotion modes smoothly, which demonstrates its adaptation capability to complex terrains, mediums, and environments. The water, narrow space, rocky terrains, barriers, and slope are conquered by the crawling, tumbling, and climbing locomotion of MR^2. The amphibious crawling motion of MR^2 is propelled by the rectangular wave with speed ranging from 5.17 mm$\cdot$ s^{-1} to 84.10 mm $\cdot$ s^{-1} (3.50 bodylength/s). The agile turning locomotion of MR ^{2} is led by the changing horizontal global magnetic component with a turning speed of 25°/s at 1 Hz. The robust tumbling locomotion of MR^2 is triggered by a rotating magnetic field with a tumbling speed of 68.98 mm$\cdot$ s^{-1} (2.87 bodylength/s) at 1 Hz to conquer the barrier of 20 mm in height and a slope of 25°. And the climbing locomotion of MR^2 is provoked by the normal global magnetic field to the robot to climb up a slope of 45°. This work illustrates a proof-of-concept robot to provide inspiration and potential for applying magnetic small-scale robots in real-world applications, like medical engineering and hard-to-reach exploration. Further development of more parameters and fundamentals of this robot warrants its own follow-up study.

References

[1] I. S. M. Khalil et al., "Independent actuation of two-tailed microrobots," *IEEE Robot. Automat. Lett.*, vol. 3, no. 3, pp. 1703–1710, Jul. 2018.

[2] Q. Ze et al., "Spinning-enabled wireless amphibious origami millirobot," *Nature Commun.*, vol. 13, no. 1, 2022, Art. no. 3118.

[3] D. Ahmed et al., "Bioinspired acousto-magnetic microswarm robots with upstream motility," *Nature Mach. Intell.*, vol. 3, pp. 116–124, Feb. 2021.

[4] J. Zhang et al., "Liquid crystal elastomer-based magnetic composite films for reconfigurable shape-morphing soft miniature machines," *Adv. Mater.*, vol. 33, no. 8, 2021, Art. no. 2006191.

[5] C. Li, S. Misra, and I. S. Khalil, "Closed-loop control characterization of untethered small-scale helical device in physiological fluid with dynamic flow rates," *Adv. Intell. Syst.*, vol. 5, no. 5, 2023, Art. no. 2200322.

[6] L. N. Pham et al., "Dexterous magnetic manipulation of conductive non-magnetic objects," *Nature*, vol. 598, no. 7881, pp. 439–443, 2021.

[7] P. Shokrollahi et al., "Blindly controlled magnetically actuated capsule for noninvasive sampling of the gastrointestinal microbiome," *IEEE/ASME Trans. Mechatronics*, vol. 26, no. 5, pp. 2616–2628, Oct. 2021.

[8] J. Yu et al., "Ultra-extensible ribbon-like magnetic microswarm," *Nature Commun.*, vol. 9, no. 1, 2018, Art. no. 3260.

[9] J. Zhang, Y. Guo, W. Hu, and M. Sitti, "Wirelessly actuated thermo-and magneto-responsive soft bimorph materials with programmable shape-morphing," *Adv. Mater.*, vol. 33, no. 30, 2021, Art. no. 2100336.

[10] H. Lu et al., "A bioinspired multilegged soft millirobot that functions in both dry and wet conditions," *Nature Commun.*, vol. 9, no. 1, 2018, Art. no. 3944.

[11] C. Huang et al., "Multimodal locomotion and cargo transportation of magnetically actuated quadruped soft microrobots," *Cyborg Bionic Syst.*, vol. 2022, Jan. 2022, Art. no. 0004.

[12] D. Hua, X. Liu, S. Sun, M. A. Sotelo, Z. Li, and W. Li, "A magnetorheological fluid-filled soft crawling robot with magnetic actuation," *IEEE/ASME Trans. Mechatronics*, vol. 25, no. 6, pp. 2700–2710, Dec. 2020.

[13] S. Wu et al., "Symmetry-breaking actuation mechanism for soft robotics and active metamaterials," *ACS Appl. Mater. Interfaces*, vol. 11, no. 44, pp. 41649–41658, 2019.

[14] Y. Wang, X. Du, H. Zhang, Q. Zou, J. Law, and J. Yu, "Amphibious miniature soft jumping robot with on-demand in-flight maneuver," *Adv. Sci.*, vol. 10, no. 18, 2023, Art. no. 2207493.

[15] I. S. Khalil, A. Klingner, Y. Hamed, Y. S. Hassan, and S. Misra, "Controlled noncontact manipulation of nonmagnetic untethered microbeads orbiting two-tailed soft microrobot," *IEEE Trans. Robot.*, vol. 36, no. 4, pp. 1320–1332, Aug. 2020.

[16] C. Zhang et al., "A manta ray-inspired biosyncretic robot with stable controllability by dynamic electric stimulation," *Cyborg Bionic Syst.*, vol. 2022, Jul. 2022, Art. no. 9891380.

[17] Y. Wang et al., "Ultrafast miniature robotic swimmers with upstream motility," *Cyborg Bionic Syst.*, vol. 4, Jan. 2023, Art. no. 0015.

[18] J. Law et al., "Gravity-resisting colloidal collectives," *Sci. Adv.*, vol. 8, Nov. 2022, Art. no. eade3161.

[19] C. Xu et al., "Magnetic miniature actuators with six-degrees-of-freedom multimodal soft-bodied locomotion," *Adv. Intell. Syst.*, vol. 4, no. 4, 2022, Art. no. 2100259.

[20] Y. Ju et al., "Reconfigurable magnetic soft robots with multimodal locomotion," *Nano Energy*, vol. 87, 2021, Art. no. 106169.

[21] Q. Ze et al., "Soft robotic origami crawler," *Sci. Adv.*, vol. 8, no. 13, 2022, Art. no. eabm7834.

[22] S. Yuan et al., "Versatile motion generation of magnetic origami spring robots in the uniform magnetic field," *IEEE Robot. Automat. Lett.*, vol. 7, pp. 10486–10493, Oct. 2022.

[23] C. J. Cai et al., "Diversified and untethered motion generation via crease patterning from magnetically actuated caterpillar-inspired origami robot," *IEEE/ASME Trans. Mechatronics*, vol. 26, no. 3, pp. 1678–1688, Jun. 2021.

[24] Q. Hu, J. Li, E. Dong, and D. Sun, "Soft scalable crawling robots enabled by programmable origami and electrostatic adhesion," *IEEE Robot. Automat. Lett.*, vol. 8, no. 4, pp. 2365–2372, Apr. 2023.

[25] J. Zhang, J. Tian, D. Zhu, Y. Liu, and S. Prasad, "Design and experimental investigation of a vibro-impact self-propelled capsule robot with orientation control," in *Proc. IEEE Int. Conf. Robot. Automat.*, 2022, pp. 11381–11387.

[26] J. Zhang et al., "Simulation and experimental studies of a vibro-impact capsule system driven by an external magnetic field," *Nonlinear Dyn.*, vol. 109, no. 3, pp. 1501–1516, 2022.

[27] H.-W. Tung, M. Maffioli, D. R. Frutiger, K. M. Sivaraman, S. Pané, and B. J. Nelson, "Polymer-based wireless resonant magnetic microrobots," *IEEE Trans. Robot.*, vol. 30, no. 1, pp. 26–32, Feb. 2014.

[28] D. R. Frutiger, B. E. Kratochvil, and B. J. Nelson, "Magmites-microrobots for wireless microhandling in dry and wet environments," in *Proc. IEEE Int. Conf. Robot. Automat.*, 2010, pp. 1112–1113.

[29] D. R. Frutiger, B. E. Kratochvil, K. Vollmers, and B. J. Nelson, "Magmites-wireless resonant magnetic microrobots," in *Proc. IEEE Int. Conf. Robot. Automat.*, 2008, pp. 1770–1771.

[30] D. R. Frutiger et al., "Small, fast, and under control: Wireless resonant magnetic micro-agents," *Int. J. Robot. Res.*, vol. 29, no. 5, pp. 613–636, 2010.

[31] Y. Liu et al., "The vibro-impact capsule system in millimetre scale: Numerical optimisation and experimental verification," *Meccanica*, vol. 55, pp. 1885–1902, 2020.

[32] K.-T. Nguyen et al., "The effect of friction on the vibro-impact locomotion system: Modeling and dynamic response," *Meccanica*, vol. 56, pp. 2121–2137, 2021.

[33] M. Salehizadeh and E. Diller, "Three-dimensional independent control of multiple magnetic microrobots via inter-agent forces," *Int. J. Robot. Res.*, vol. 39, no. 12, pp. 1377–1396, 2020.

[34] J. Zhang, M. Salehizadeh, and E. Diller, "Parallel pick and place using two independent untethered mobile magnetic microgrippers," in *Proc. IEEE Int. Conf. Robot. Automat.*, 2018, pp. 123–128.

Authorized licensed use limited to: The University of Hong Kong Libraries. Downloaded on October 03,2024 at 16:21:31 UTC from IEEE Xplore. Restrictions apply.